Regional exploration of crustal structures from long-offset OBN data by extended-source FWI

*Gaoshan Guo *, Stéphane Operto**
**Université Côte d'Azur-CNRS-IRD-OCA, Geoazur, Valbonne, France*

SUMMARY

Regional seismic imaging of continental margins from ultra long-offset sparse ocean-bottom node (OBN) data by Full-waveform inversion (FWI) is challenging because the complexity of the wavefields and the large number of propagated wavelengths significantly amplify the nonlinearity of the inverse problem. Moreover, the sparsity of OBN deployments mitigates the fold and can induce aliasing artifacts in the shallow part of the model. In this context, deriving a sufficiently-accurate initial model that prevents cycle skipping is difficult. We circumvent this challenge with time-domain extended-source (ES-) FWI combined with total variation regularization. ES-FWI first estimates at each iteration the scattering sources of the scattered wavefield by the sought perturbation model by fitting the data residuals (the scattered data) before updating the subsurface model toward the true model by minimizing the scattering sources (wave-equation errors). Accordingly, data are matched arbitrarily well and cycle skipping is avoided. We design a practical time-domain acoustic ES-FWI workflow from synthetic OBN data computed in a regional geomodel of a subduction zone. This study demonstrates that ES-FWI can effectively converge towards precise reconstruction of complex geological structure starting from basic 1D model with severe cycle-skipping. Source-focusing and data-domain weighting matrices in the bi-objective function are however two necessary ingredients to design a layer-stripping scheme that greatly enhances the robustness of ES-FWI.

INTRODUCTION

Long-offset controlled-source stationary-recording seismic surveys carried out with Ocean-Bottom Nodes (OBN) are widely used for the regional deep-offshore exploration of continental margins. For such crustal surveys, the predominant approach for determining large-scale crustal structures still relies on traveltime tomography (see Christeson et al. (2014) for a Gulf of Mexico case study). Alternatively, full waveform inversion (FWI) leverages the entire dataset to build subsurface models with a wavelength resolution (Virieux and Operto, 2009). While FWI has emerged as the fundamental technique for characterizing subsurface structures in the realm of oil/gas exploration (Sirgue et al., 2010), its application to OBN data at the regional scale remains infrequent (Górszczyk et al., 2017, 2021). One of the primary challenges in applying standard FWI to crustal-scale seismic imaging is the cycle-skipping problem, which traps FWI in spurious minima when the simulated data in the initial model don't match the observed data with an error of less than half the minimum period. This problem becomes particularly pronounced when dealing with ultra long-offset OBN data that involve many propagated wavelengths. Building kinematically accurate initial model for crustal-scale FWI requires careful quality control of traveltime picking and traveltime tomography results, which can be quite time consuming (Górszczyk et al., 2017). Moreover, data-driven hierarchical schemes based on frequency, time and offset continuation are often necessary to further mitigate FWI non linearity (Shipp and Singh, 2002; Górszczyk et al., 2017).

In recent decades, significant progress has been made to mitigate cycle skipping by convexifying FWI. One category of methods replaces the least-squares norm of the data misfit with more convex distances between observed and simulated data such as those based on optimal transport or deconvolution (e.g. Warner and Guasch, 2016; Métivier et al., 2018). Other approaches adds degrees of freedom in the forward problem to expand the search space of the inversion (Symes, 2008). This extension can be performed in the model domain (Barnier et al., 2023), source domain (van Leeuwen and Herrmann, 2013) and receiver domain (Métivier and Brossier, 2022). Despite the rapid development of these FWI variants, their application at the regional scale has been limited. Górszczyk et al. (2021) demonstrated the potential of using optimal transport to address the cycle skipping problem using a narrow time window of low-frequency data and complex data-driven workflow involving amplitude normalization. To date, this may represent the sole successful application of alternative cost function at the regional scale. In contrast, numerous synthetic case studies have validated the potential of extended-space approaches in exploration geophysics, while the robustness at the regional scale has yet to be proven. This study aims at filling this gap with an application of extended-source(ES)-FWI (Gholami et al., 2022; Guo et al., 2024) to the regional GO_3D_OBS geomodel (Górszczyk and Operto, 2021). This feasibility analysis is the prerequisite before the application to real OBN data for regional exploration (Górszczyk et al., 2017, 2021).

METHOD

FWI is formulated as a nonlinear multivariate partial differential equation (PDE)-constrained optimization problem:

$$\min_{\mathbf{u}_s,\mathbf{m}} \sum_s \|\mathbf{P}_s\mathbf{u}_s - \mathbf{d}_s^*\|_2^2 \ \text{ s.t. } \ \mathbf{A}(\mathbf{m})\mathbf{u}_s = \mathbf{b}_s^*, \ \text{ for all s,} \qquad (1)$$

where s is the source index, $\mathbf{u}_s$ is the wavefield triggered by the source s, $\mathbf{d}_s^*$ is the recorded data for the source s, $\mathbf{b}^*$ is the physical source s, $\mathbf{P}_s$ samples $\mathbf{u}_s$ at receiver locations, $\mathbf{A}(\mathbf{m})$ is the wave equation operator. In the following, we drop the summation over s for the sake of compact notation. Wavefield reconstruction inversion (WRI) recasts the original multivariate constrained problem, equation 1, as the following unconstrained problem with a penalty function (van Leeuwen and Herrmann, 2013),

$$\min_{\mathbf{u}_s,\mathbf{m}} \mathscr{P}_\mu(\mathbf{u}_s,\mathbf{m}) = \frac{1}{2}\|\mathbf{P}_s\mathbf{u}_s - \mathbf{d}_s^*\|_2^2 + \frac{\mu}{2}\|\mathbf{A}(\mathbf{m})\mathbf{u}_s - \mathbf{b}_s^*\|_2^2, \quad (2)$$

where μ is the penalty parameter. The penalty function performs a relaxation of the wave equation that allows one to fit the data arbitrarily well through the tuning of μ. This bivariate problem can be solved with alternating directions or by

variable projection (van Leeuwen and Herrmann, 2016). However, the implementation of WRI in the time domain is challenging because the wavefield in equation 2 is the solution of a normal equation. To address this issue, Gholami et al. (2022); Operto et al. (2023) reformulate the wavefield reconstruction problem as a scattering source problem after the change of variable $\mathbf{u}_s \rightarrow \delta\mathbf{b}_s$ where $\mathbf{A}(\mathbf{m})\mathbf{u}_s - \mathbf{b}_s = \delta\mathbf{b}_s$. The problem 2 becomes

$$\min_{\delta\mathbf{b}_s,\mathbf{m}} \mathscr{P}_\mu(\delta\mathbf{b}_s,\mathbf{m}) = \frac{1}{2}\|\mathbf{S}_s(\mathbf{m})\delta\mathbf{b}_s - \delta\mathbf{d}_s^*\|_2^2 + \frac{\mu}{2}\|\delta\mathbf{b}_s\|_2^2.$$

where $\mathbf{S}_s(\mathbf{m}) = \mathbf{P}_s\mathbf{A}(\mathbf{m})^{-1}$ and $\delta\mathbf{d}_s^* = \mathbf{P}_s\mathbf{u}_s - \mathbf{d}_s^*$. Furthermore, Guo et al. (2024) introduce a generalized cost function for time-domain ES-FWI:

$$\min_{\delta\mathbf{b}_s,\mathbf{m}} \mathscr{P}_\mu(\delta\mathbf{b}_s,\mathbf{m}) = \frac{1}{2}\|\mathbf{S}_s(\mathbf{m})\delta\mathbf{b}_s - \delta\mathbf{d}_s^*\|_{\mathbf{Q}_{d_s}}^2 + \frac{\mu}{2}\|\delta\mathbf{b}_s\|_{\mathbf{Q}_{b_s}}^2, \tag{3}$$

where $\mathbf{Q}_d$ and $\mathbf{Q}_b$ denote data-domain and source-domain weighting matrices, respectively. Let's focus first on the lower-level problem for $\delta\mathbf{b}_s^e$ as the minimizer of the monovariate objective function considering $\mathbf{m}$ fixed. According to Tarantola (2005, equation 6.525), the closed-formed expression of $\delta\mathbf{b}_s^e(\mathbf{m})$ is given by

$$\delta\mathbf{b}_s^e(\mathbf{m}) = \mathbf{Q}_{b_s}^{-1}\mathbf{S}_s(\mathbf{m})^T\mathbf{Q}_{d_s}\mathbf{H}(\mathbf{m})_{d_s}^{-1}\delta\mathbf{d}_s^*(\mathbf{m}), \tag{4}$$

where the weighted data-domain Hessian is given by

$$\mathbf{H}(\mathbf{m})_{d_s} = \mu\mathbf{I} + \mathbf{S}_s(\mathbf{m})\mathbf{Q}_{b_s}^{-1}\mathbf{S}_s(\mathbf{m})^T\mathbf{Q}_{d_s}. \tag{5}$$

The computation of this data-domain Hessian is the main bottleneck of time-domain ES-FWI. Gholami et al. (2022) and Guo et al. (2024) approximate it by a scaled identify matrix and by matching filters, respectively. Finally, $\mathbf{u}_s^e$ can be computed with explicit time-stepping schemes by solving the wave equation $\mathbf{A}(\mathbf{m})\mathbf{u}_s^e = \mathbf{b}_s^* + \delta\mathbf{b}_s^e(\mathbf{m})$. The gradient of $\mathscr{P}_\mu(\delta\mathbf{b},\mathbf{m})$ *.wrt.* $\mathbf{m}$ is the gradient of the $\ell 2$ norm of the scattering source:

$$\nabla_{\mathbf{m}}\mathscr{P}_\mu(\delta\mathbf{b},\mathbf{m})|_{\delta\mathbf{b}^e} = \sum_s \left(\frac{\partial\mathbf{A}(\mathbf{m})\mathbf{u}_s^e}{\partial\mathbf{m}}\right)^T \mathbf{Q}_{b_s}\delta\mathbf{b}_s^e(\mathbf{m}) \tag{6}$$

The Gauss-Newton Hessian reduces to the weighted correlation of the extended-space virtual sources

$$\nabla_{\mathbf{m}}^2\mathscr{P}_\mu(\mathbf{m}) = \sum_s \left(\frac{\partial\mathbf{A}(\mathbf{m})\mathbf{u}_s^e}{\partial\mathbf{m}}\right)^T \mathbf{Q}_b^T \left(\frac{\partial\mathbf{A}(\mathbf{m})\mathbf{u}_s^e}{\partial\mathbf{m}}\right). \tag{7}$$

We implement $\mathbf{Q}_b$ as a spatial source-focusing function to penalize more strongly scattering sources that are far away from the point source position following the annihilator approach promoted by Huang et al. (2018); Rizzuti et al. (2021),

$$\mathbf{Q}_b(\mathbf{x}) = \sqrt{(\mathbf{x}-\mathbf{x}_s)^2}, \tag{8}$$

where $\mathbf{x}_s$ denotes the position of the source s. The variance assigned to the source extension away from the sources becomes increasingly small hence damping the perturbation of the source extensions away from the source. This is shown by the expression of the Newton descent direction for $\delta\mathbf{b}$ which is scaled by the inverse of $\mathbf{Q}_b$, equation 4. On the other hand, we design $\mathbf{Q}_d$ as a combination of time and offset windowing to implement a layer stripping approach (Górszczyk et al., 2017), which allows us to easily control the data subset injected in the inversion. This is combined with a classical frequency continuation approach leading to the multi-scale ES-FWI algorithm. To avoid tedious adaptive tuning of μ, we implement ES-FWI with an augmented Lagrangian function, which combines the penalty function, equation 2, with a Lagrangian function (Gholami et al., 2022; Guo et al., 2024).

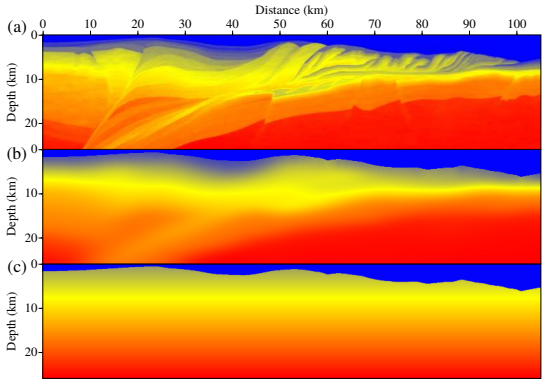

Figure 1: GO_3D_OBS benchmark. (a) True model. (b) Smoothed initial model. (c) 1D initial model.

Numerical tests

Experimental setup

We illustrate how ES-FWI mitigates the detrimental impact of cycle-skipping of ultra long-offset OBN data with a 2D section of the GO_3D_OBS geomodel. This geomodel represents a subduction zone inspired by the geology of the Nankai trough (Górszczyk and Operto, 2021) (Figure 1a). The role of the weighing operators in ES-FWI is illustrated with two initial models: the first one is generated by smoothing the true model with a Gaussian filter of correlation lengths 1.8 km$\times$ 4.2 km (Figure 1b). This model contains the long wavelengths of the true model but it is not accurate enough to avoid cycle skipping for the considered frequency bandwidth. The second is a linear gradient 1D model that doesn't contain a priori information about the true model (Figure 1c) with the exception of the water wavespeed and bathymetry. The acquisition involves 100 OBNs on the seabed spaced 1 km apart and 1040 shots spaced 100 m apart at 50-m depth below sea surface. OBNs and shots are processed as reciprocal sources and receivers, respectively. We perform wave simulation with a finite-difference time-domain modeling engine using a 28 s recording length and a 2 Hz Ricker wavelet. ES-FWI is performed within the $(1.5,\ 4)$ Hz frequency band. We implement a free-surface boundary condition at the sea/air interface and perfectly matched layer (PML) absorbing condition on the remaining sides of the model. We recall that we use total variation regularization (Aghamiry et al., 2019) to carry out these two tests. Moreover, we approximate the inverse data-domain Hessian with a 2D Gabor filter (Guo et al., 2024).

Results

Smooth initial model: On the effect of source-focusing

We first compare classical FWI and ES-FWI using the smoothed initial model depicted in Figure 1b. For this test, we use only the source-focusing function, equation 8, as a weighting oper-

ator in the generalized ES-FWI, equation 3. The configuration of the multi-scale inversion is outlined in Table 1. First, we

Table 1: Smoothed initial model. Outline of inversion steps. *freq*: frequency band involved in inversion. *grid*: grid sizes. Grid interval is matched to minimum wavelength. *#it*: number of iterations.

Scale	freq (Hz)	grid (nz × nx × nt)	#it
1 (ES-FWI)	1.5-1.8	173 × 701 × 2801	42
2 (ES-FWI)	1.5-2.0	173 × 701 × 2801	31
3 (ES-FWI)	1.5-2.8	259 × 1041 × 4001	44
4 (FWI)	1.5-4.0	345 × 1401 × 5601	112

assess data match at the first scale using classical FWI and ES-FWI. Significant cycle-skipping between recorded and simulated data is obvious in Figure 2a. Accordingly, FWI converges towards an incorrect model due to cycle skipping (Figure 3a). Moreover, ES-FWI converges towards a spurious minimum when the source-focusing function is not used ($\mathbf{Q}_b$, equation 8) (Figure 3b). Compared with the result of FWI (Figure 2b), the short-offset data of ES-FWI could align with observed data (Figure 2c). However, the data recorded at offsets greater than 20 km are still cycle-skipped, because the approximation of the inverse data-domain Hessian with a 2D matching filter is not precise enough. Rather than paying the price of the computational cost of improving the accuracy of the inverse data-domain Hessian, we introduce the source-focusing function to ES-FWI without additional computational burden. As shown in Figure 3c, the long-wavelength structure is reconstructed well by ES-FWI with a source-focusing function. Despite this achievement, long-offset data ranging from 80 to 100 km continue to be cycle skipped (Figure 2c), and the deep structure beneath the subducting crust remains imprecise. This source-focusing function could partly compensate for the inaccuracy of data-domain Hessian, especially for such large-scale crustal ES-FWI. Then, starting from the final model of the first-scale ES-FWI with source focusing, we initiate the second-scale inversion with the same approach. The final model of the second scale inversion is shown in Figure 4a. Upon completing the third-scale inversion using ES-FWI with source-focusing, the deeper structure is well-reconstructed (Figure 4b). Lastly, we switch from ES-FWI to FWI in the fourth-scale inversion to further refine the structure (Figure 4c).

Crude initial model: On the effect of time-offset windowing
We proceed now with the second test using the 1D linear initial model (Figure 1c). The configuration of the multi-scale inversion with layer stripping ($\mathbf{Q}_d$ and $\mathbf{Q}_b$ are used) is outlined in Table 2. In a similar manner, we show the data match between the simulated data in the 1D linear model and the observed data at the first-scale step, where the data mismatch spans several cycles (Figure 5a). Starting from this crude initial model, ES-FWI with a source-focusing function struggles to converge towards an accurate model (Figure 6a), and the data mismatch remains substantial (Figure 5b). However, when we introduce a data-domain time-offset windowing in ES-FWI combined with a source-focusing function, we can progressively involve more complex data in the inversion process and better control the level of hierarchy with which the model is updated from the shallow parts to the deeper parts (Figure 6b), ultimately

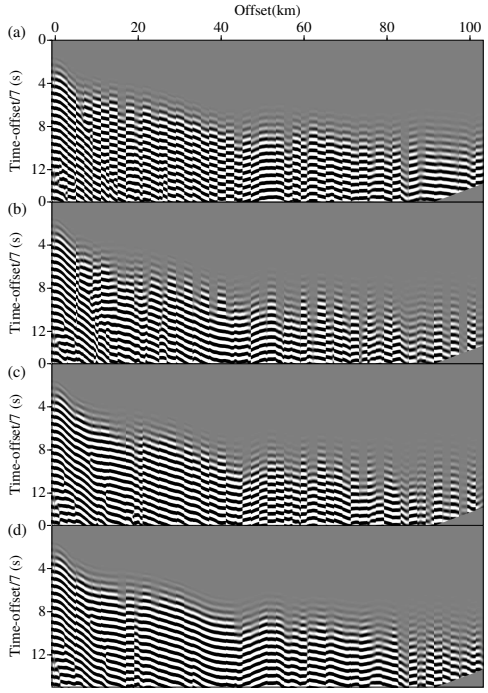

Figure 2: Smoothed initial model. Data fit after the first-scale inversion. (a-d) Interleaved observed data and simulated data in (a) the initial model (Figure 1b), (b-d) the inverted model using (b) FWI (Figure 3a), (c) ES-FWI without $\mathbf{Q}_b$ (Figure 3b) with $\mathbf{Q}_b$ (Figure 3c).

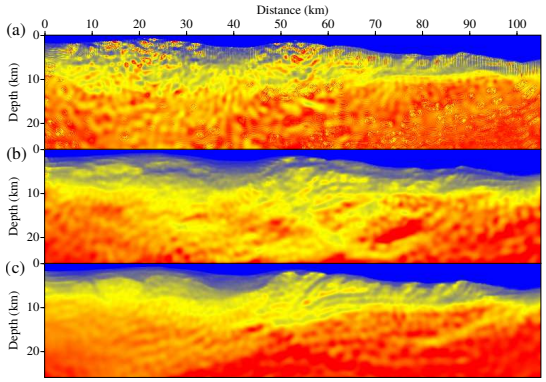

Figure 3: Smoothed initial model. Final models of first-scale inversion. (a-c) Reconstructed model using (a) FWI, (b-c) ES-FWI without (b) and with (c) $\mathbf{Q}_b$.

leading to a much improved solution. The time windows defined from the first-arrival traveltimes and the maximum offset involved in each inversion step are outlined in Table 2. Simulated data now closely aligns with observed data, even at long offsets (Figure 5c). Subsequently, we proceed with the second scale (Figure 7a) and the third scale (Figure 7b) by processing the entire dataset in one go, without data weighting using generalized ES-FWI with $\mathbf{Q}_b$. In the final scale, we employ classical FWI to further refine the structure of the subduction zone (Figure 7c).

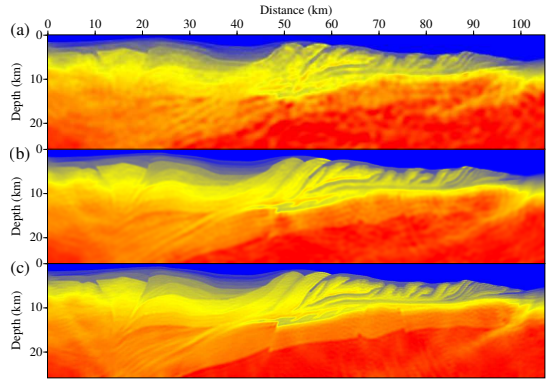

Figure 4: Smoothed initial model. Multi-scale inversion starting from the final model of the first-scale inversion (Figure 3c). (a-b) Final model of second-scale (a) and third-scale (b) inversion by generalized ES-FWI with $\mathbf{Q}_b$. (c) Final model of fourth-scale inversion by FWI.

Table 2: 1D initial model. Outline of inversion steps. T: time window from first arrival involved in inversion. O: maximum offset involved in inversion. Spatial and temporal sampling for each scale are the same as those of Table 1.

Scale	freq (Hz)	iterations	T (s)	O (km)
1 (ES-FWI)	1.5-1.8	42	5	5
1 (ES-FWI)	1.5-1.8	42	6	6
1 (ES-FWI)	1.5-1.8	23	6	12
1 (ES-FWI)	1.5-1.8	32	6	24
1 (ES-FWI)	1.5-1.8	32	7	36
1 (ES-FWI)	1.5-1.8	32	7	120
2 (ES-FWI)	1.5-2.0	101	all	all
3 (ES-FWI)	1.5-2.8	84	all	all
4 (FWI)	1.5-4.0	42	all	all

CONCLUSIONS

We assess up to which point ES-FWI allows one to relax all the necessary specifications that need to be fulfilled to make crustal-scale FWI work in a challenging context. According to recent studies, these specifications are a kinematically accurate starting model regarding the smallest available frequency, frequency continuation, and layer stripping by time-offset windowing. We show that these specifications are still beneficial for ES-FWI. However, the need for a highly accurate traveltime picking and starting model with tedious quality control, which is probably the most time-consuming and complex task, can be probably relaxed when using ES-FWI. This can mitigate significantly human intervention and tend toward a more automatic use of FWI. This synthetic benchmark allows us to set up different ingredients (covariance matrices and layer stripping scheme by time-offset windowing) which can be useful to make ES-FWI more robust in very complex settings. The next step was the application on real data with the issue of the specific tuning of these ingredients for a real case study.

Acknowledgments: This study was funded by the WIND consortium (www.geoazur.fr/WIND). This study was granted access to the HPC resources of SIGAMM and the HPC resources of GENCI under the allocation 0596.

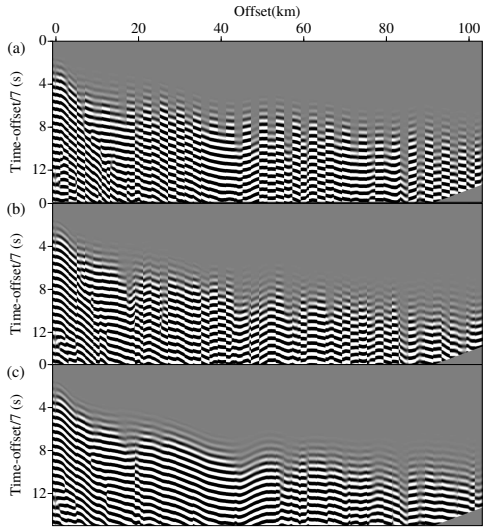

Figure 5: 1D initial model. Data fit after first-scale inversion. (a-d) Interleaved data between observed data and simulated data in (a) initial model (Figure 1c), (b-c) the final model inferred from generalized ES-FWI using (b) $\mathbf{Q}_b$ only (Figure 6a), (c) $\mathbf{Q}_b$ and $\mathbf{Q}_d$ (Figure 6b).

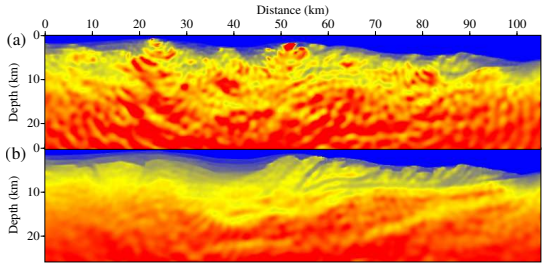

Figure 6: 1D initial model. Final models of first-scale inversion. (a-b) Reconstructed model by generalized ES-FWI with (a) $\mathbf{Q}_b$ only, (b) $\mathbf{Q}_b$ and $\mathbf{Q}_d$.

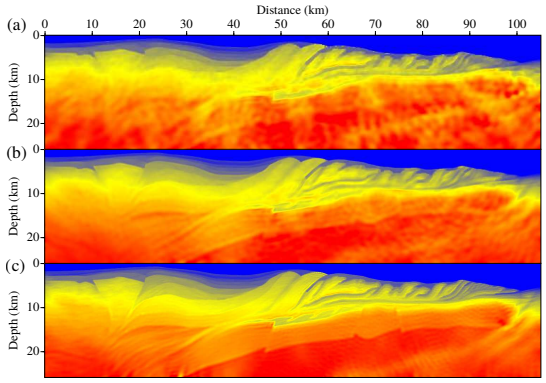

Figure 7: 1D initial model. Multi-scale inversion starting from the final model of the first-scale inversion (Figure 6g). (a-b) Model inferred from the second-scale (a) and third-scale (b) inversion using generalized ES-FWI with $\mathbf{Q}_b$. (c) Final model of fourth-scale inversion using FWI.

REFERENCES

Aghamiry, H., A. Gholami, and S. Operto, 2019, Implementing bound constraints and total-variation regularization in extended full waveform inversion with the alternating direction method of multiplier: application to large contrast media: Geophysical Journal International, **218**, 855–872.

Barnier, G., E. Biondi, R. G. Clapp, and B. Biondi, 2023, Full-waveform inversion by model extension: Theory, design, and optimization: GEOPHYSICS, **88**, R579–R607.

Christeson, G. L., H. J. A. V. Avendonk, I. O. Norton, J. W. Snedden, D. R. Eddy, G. D. Karner, and C. A. Johnson, 2014, Deep crustal structure in the eastern Gulf of Mexico: Journal of Geophysical Research: Solid Earth, **119**, 6782–6801.

Gholami, A., H. S. Aghamiry, and S. Operto, 2022, Extended full waveform inversion in the time domain by the augmented Lagrangian method: Geophysics, **87**, R63–R77.

Górszczyk, A., R. Brossier, and L. Mtivier, 2021, Graph-space optimal transport concept for time-domain full-waveform inversion of ocean-bottom seismometer data: Nankai trough velocity structure reconstructed from a 1D model: Journal of Geophysical Research: Solid Earth, **126**, e2020JB021504.

Górszczyk, A., and S. Operto, 2021, GO_3D_OBS: the multi-parameter benchmark geomodel for seismic imaging method assessment and next-generation 3D survey design (version 1.0): Geoscientific Model Development, **14**, 17731799.

Górszczyk, A., S. Operto, and M. Malinowski, 2017, Toward a robust workflow for deep crustal imaging by FWI of OBS data: The eastern Nankai trough revisited: Journal of Geophysical Research: Solid Earth, **122**, 4601–4630.

Guo, G., S. Operto, A. Gholami, and H. S. Aghamiry, 2024, Time-domain extended-source full-waveform inversion: algorithm and practical workflow: Geophysics, **89(2)**, 1–22.

Huang, G., R. Nammour, and W. W. Symes, 2018, Source-independent extended waveform inversion based on space-time source extension: Frequency-domain implementation: Geophysics, **83**, R449–R461.

Métivier, L., A. Allain, R. Brossier, Q. Mérigot, E. Oudet, and J. Virieux, 2018, Optimal transport for mitigating cycle skipping in full waveform inversion: a graph space transform approach: Geophysics, **83**, R515–R540.

Métivier, L., and R. Brossier, 2022, Receiver-extension strategy for time-domain full-waveform inversion using a relocalization approach: Geophysics, **87**, R13–R33.

Operto, S., A. Gholami, H. S. Aghamiry, G. Guo, , S. Beller, K. Aghazade, F. Mamfoumbi, L. Combe, and A. Ribodetti, 2023, Extending the search space of FWI beyond the single-scattering Born approximation: Geophysics, **88(6)**, R671–R702.

Rizzuti, G., M. Louboutin, R. Wang, and F. J. Herrmann, 2021, A dual formulation of wavefield reconstruction inversion for large-scale seismic inversion: Geophysics, **86**, R879–R893.

Shipp, R. M., and S. C. Singh, 2002, Two-dimensional full wavefield inversion of wide-aperture marine seismic streamer data: Geophysical Journal International, **151**, 325–344.

Sirgue, L., O. I. Barkved, J. Dellinger, J. Etgen, U. Albertin, and J. H. Kommedal, 2010, Full waveform inversion: the next leap forward in imaging at Valhall: First Break, **28**, 65–70.

Symes, W. W., 2008, Migration velocity analysis and waveform inversion: Geophysical Prospecting, **56**, 765–790.

Tarantola, A., 2005, Inverse Problem Theory and Methods for Model Parameter Estimation: Society for Industrial and Applied Mathematics.

van Leeuwen, T., and F. Herrmann, 2016, A penalty method for PDE-constrained optimization in inverse problems: Inverse Problems, **32(1)**, 1–26.

van Leeuwen, T., and F. J. Herrmann, 2013, Mitigating local minima in full-waveform inversion by expanding the search space: Geophysical Journal International, **195(1)**, 661–667.

Virieux, J., and S. Operto, 2009, An overview of full waveform inversion in exploration geophysics: Geophysics, **74**, WCC1–WCC26.

Warner, M., and L. Guasch, 2016, Adaptive waveform inversion: Theory: Geophysics, **81**, R429–R445.